Acta Materialia 95 (2015) 20–29

Contents lists available at ScienceDirect

Acta Materialia

journal homepage: www.elsevier.com/locate/actamat

# Effect of Ag on interfacial segregation in Mg–Gd–Y–(Ag)–Zr alloy

H. Zhou [a,b], G.M. Cheng [b], X.L. Ma [b], W.Z. Xu [b], S.N. Mathaudhu [c], Q.D. Wang [a,*], Y.T. Zhu [b,d,*]

[a] National Engineering Research Center of Light Alloys, Net Forming and State Key Laboratory of Metal Matrix Composite, Shanghai Jiao Tong University, 200240 Shanghai, PR China
[b] Department of Materials Science & Engineering, North Carolina State University, Raleigh, NC 27695, USA
[c] Department of Mechanical Engineering, University of California, Riverside, CA 92521, USA
[d] School of Materials Science and Engineering, Nanjing University of Science and Technology, Nanjing 210094, PR China

ARTICLE INFO

*Article history:*
Received 12 January 2015
Revised 12 May 2015
Accepted 17 May 2015
Available online 31 May 2015

*Keywords:*
Magnesium alloys
Interface
Segregation
HAADF-STEM
Crystal structure

ABSTRACT

Interfaces such as twin boundaries, stacking faults and grain boundaries often play an important role in controlling mechanical properties of metals through interaction with dislocations. Segregation of alloy elements and impurities to these interfaces can stabilize them and produce a large strengthening effect. Here we report the effect of Ag on segregation of alloy elements at twin boundaries, stacking faults and grain boundaries in the Mg–Gd system. Specifically, for the first time a spinal-shaped periodic segregation is observed at the $\{1\,0\bar{1}2\}$ twin boundary and high-angle lamellar grain boundary in the Mg–Gd–Y–Zr alloy due to the presence of the Ag addition. The segregation consists of Gd- and Ag-rich columns. It appears that high Ag content in the spinal-shaped segregation induces fcc-like cell structures.



## 1. Introduction

Due to their lightweight, magnesium alloys are becoming increasingly attractive for structural applications in aerospace, automotive, and electronic industries [1,2]. Extensive effort has been made to improve their mechanical strength [3], formability [4], creep resistance [5] and corrosion resistance [6]. Reported strategies to enhance strength of Mg alloys include grain refinement [7], age hardening [8,9] and introduction of stacking faults [10–12]. Moreover, by combining these strengthening mechanisms, several high-strength magnesium alloys containing rare earth elements (Mg–RE) have been developed. For example, Homma et al. [13] developed a high-strength Mg–Gd–Y–Zn–Zr alloy that has yield strength of 473 MPa by combining significant grain refinement with age hardening.

Since the solubility of the rare earth alloying elements decreases with decreasing temperature, Mg–RE alloys can be significantly hardened by precipitation of second phase particles. It has been reported that the precipitation process in Mg–Gd–Y alloy follows the sequence of S.S.S.S (Supersaturated Solid solution) → $\beta''$ → $\beta_T$ → $\beta'$ → $\beta_1$ → $\beta$ [14]. The precipitates, especially the peak aged $\beta'$ phase, enhance the mechanical strength by blocking dislocation slip [15]. Moreover, rare earth atoms tend to segregate at interfaces such as grain boundaries [16,17], twins boundaries [18], and stacking faults [19]. Such segregation is believed effective in pinning dislocations, which leads to further strengthening [20,21].

Previous studies revealed that additional Zn element in Mg–RE alloys induced a novel type of long period stacking ordered (LPSO) structures during annealing and consequently enhanced strength. This has led to a recent increase in research of magnesium alloy strengthening via this mechanism [22–27]. Interestingly, other alloying elements, such as Ag, also show similar strengthening effect in Mg–RE alloys [28]. Wang et al. [29] found that the tensile strength of as-cast Mg–Gd–Y alloys was further improved by adding ~2 wt.% of Ag. The tensile strength of peak aged Mg–Gd–Y–Ag alloy reached a high ultimate tensile strength (UTS) of 403 MPa without compromising elongation. Jian et al. [10,11] also found that the rolled Mg–Gd–Y–Ag alloy shows much higher yield strength than a Mg–Gd–Y alloy that has similar elemental composition of Gd and Y. Their hypothesis was that the induced stacking faults played a critical role in the improvement of mechanical properties. However, it is still not well understood how Ag element affects microstructure evolution of Mg–RE alloys during deformation and heat treatment.

In this work, two Mg–RE alloys with similar compositions except for Ag content were studied in order to investigate how

* Corresponding authors at: Department of Materials Science & Engineering, North Carolina State University, Raleigh, NC 27695, USA. Tel.: +1 919 513 0559 (Y.T. Zhu). Tel.: +86 21 54742715 (Q.D. Wang).
*E-mail addresses:* wangqudong@sjtu.edu.cn (Q.D. Wang), ytzhu@ncsu.edu (Y.T. Zhu).

http://dx.doi.org/10.1016/j.actamat.2015.05.020
1359-6454/

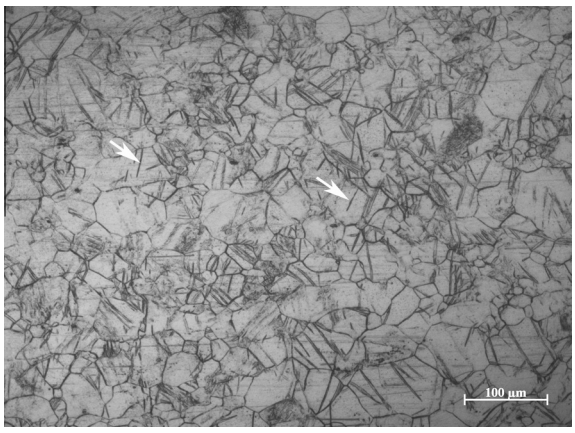


**Fig. 1.** Optical micrograph of the microstructure of the Mg–Gd–Y–(Ag)–Zr alloy subjected to 75% hot-rolling.

the Ag addition affects segregation at various interfaces such as twin boundaries, stacking faults, and grain boundaries. Atomic-scale characterization was carried out using high-angle annular dark-field (HAADF) scanning transmission electron microscopy (STEM) with an ultra-high spatial resolution of ~0.10 nm, which provided a more precise and reliable structural interpretation of chemical ordering, and a better understanding of the atomic configuration [30,31]. Since the differences in atomic numbers between the constituent elements are fairly large (Mg: 12, Gd: 64, Y: 39, Ag: 47), we were able to obtain *Z* (atomic number) – contrast images to differentiate segregated heavy solute atoms. Basing on comprehensive analysis of electron diffraction patterns, atomic resolution images and also sub-nanometer chemical analysis with energy-dispersive X-ray spectroscopy (EDS), we were able to establish models of atomic segregation at coherent twin boundaries, stacking faults and grain boundaries.

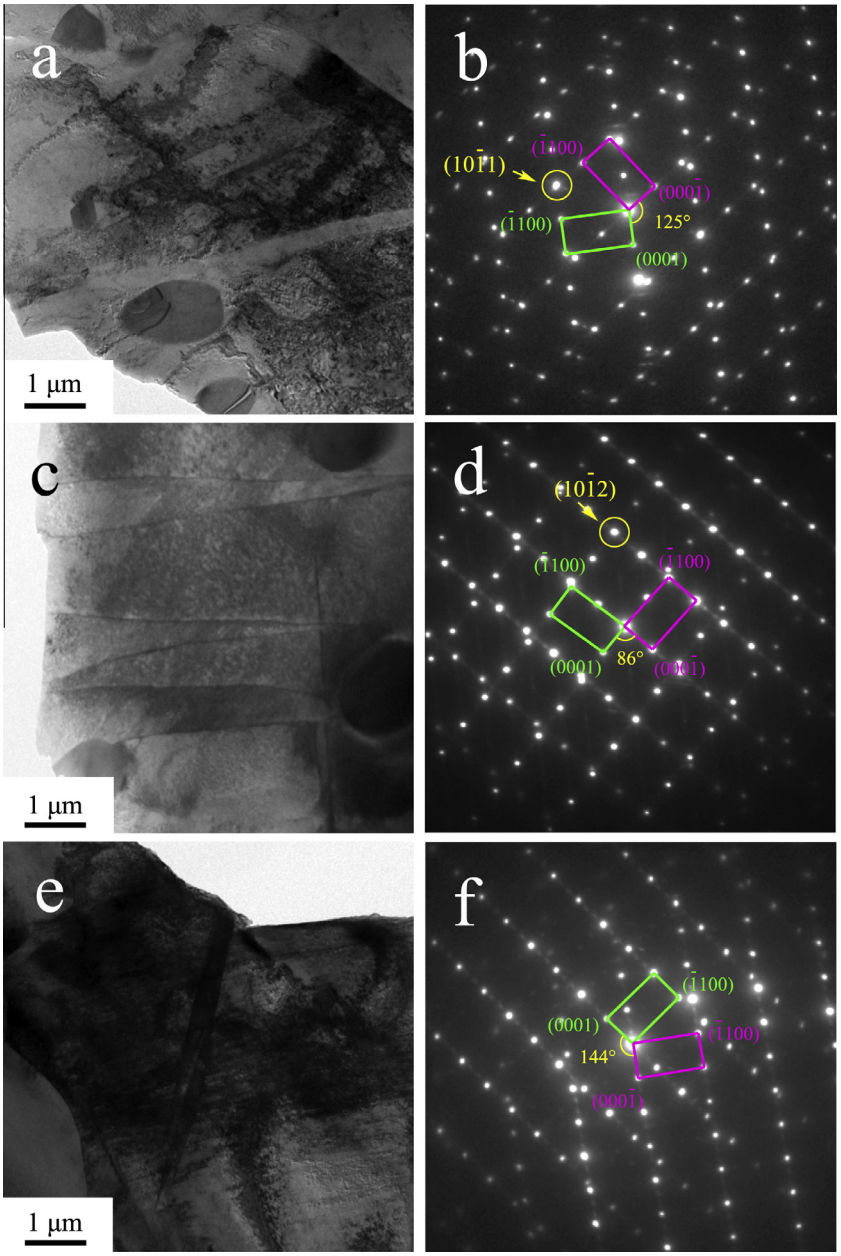


**Fig. 2.** TEM images and selected area diffraction of lamellae structures in the hot rolled Mg–Gd–Y–(Ag) alloy: (a) and (b) {10$\bar{1}$1} twin (TBI); (c) and (d) {10$\bar{1}$2} twin (TBII); and (e) and (d) lamellar grain boundary (LGB).

**Table 1**
Lamellar structures in the Mg–Gd–Y–(Ag)–Zr alloy subjected to 75% hot rolling.

| Lamellar Structures | Abbreviation | Definition | Misorientation between two {0001} planes |
|---|---|---|---|
| $\{10\bar{1}1\}$ twins | TBI | Compression twin | ~125° |
| $\{10\bar{1}2\}$ twins | TBII | Tensile twin | ~86° |
| Lamellar grain boundary | LGB | Special grain boundary | 146°, 144°, 140°, 102°, etc. |

## 2. Experimental procedures

The casting procedure used to produce the Mg–10.1Gd–3.5Y–0.45Zr and Mg–10.4Gd–1.6Y–(2.0Ag)–0.13Zr (wt.%) ingots can be found in reference [32]. For simplicity, these two alloys are hereafter referred to as the Mg–Gd–Y alloy and Mg–Gd–Y–Ag alloy, respectively. The as-cast ingots were solution treated at 500 °C for 12 h in a vacuum furnace and quenched to room temperature in silicon oil (T4 treatment). The T4-treated samples with dimensions of $20 \times 25 \times 2$ mm$^3$ were used as the starting material for hot rolling. Specimens for hot rolling were heated at 450 °C for 15 min before each rolling pass, and then rolled on a conventional hot roller with a thickness reduction of ~0.1 mm per pass and total rolling reduction of 75%. Annealing after rolling was performed at 250 °C for 0.5 h. The specimens for optical microscopy characterization were ground with sandpaper of 320, 600, and 800 grits, and then polished by a woolen cloth with 1 μm diamond suspension. Final polishing was done using magnesia suspension on polishing cloth to a mirror finish. The etching solution was comprised of 100 ml ethyl alcohol with 5 g picric acid and 5 g acetic acid. Cross-sectional TEM specimens were cut from the rolling sheet and gently polished to a thickness of ~25 μm. Perforation by ion milling was carried out on a cold stage (~−50 °C) with low angle (<3.5°) and low energy ion beam (<3 KeV). Atomic-resolution high-angle annular dark-field (HAADF) observation was conducted on an aberration-corrected scanning transmission electron microscope (STEM) (FEI Titan 80-300) operated at 200 kV. EDS mapping was conducted at an accelerating voltage of 80 kV to avoid excessive irradiation damage to the Mg alloy samples [33].

## 3. Results

### 3.1. Microstructure

The microstructure of 75% hot-rolled Mg–Gd–Y–Ag alloy is shown in Fig. 1. Straight lamellar structures were frequently observed in coarse grains (~15 μm). Previous investigations regarded them as deformation twins, which had specific orientation from parent grains [34,35]. Deformation twinning is a

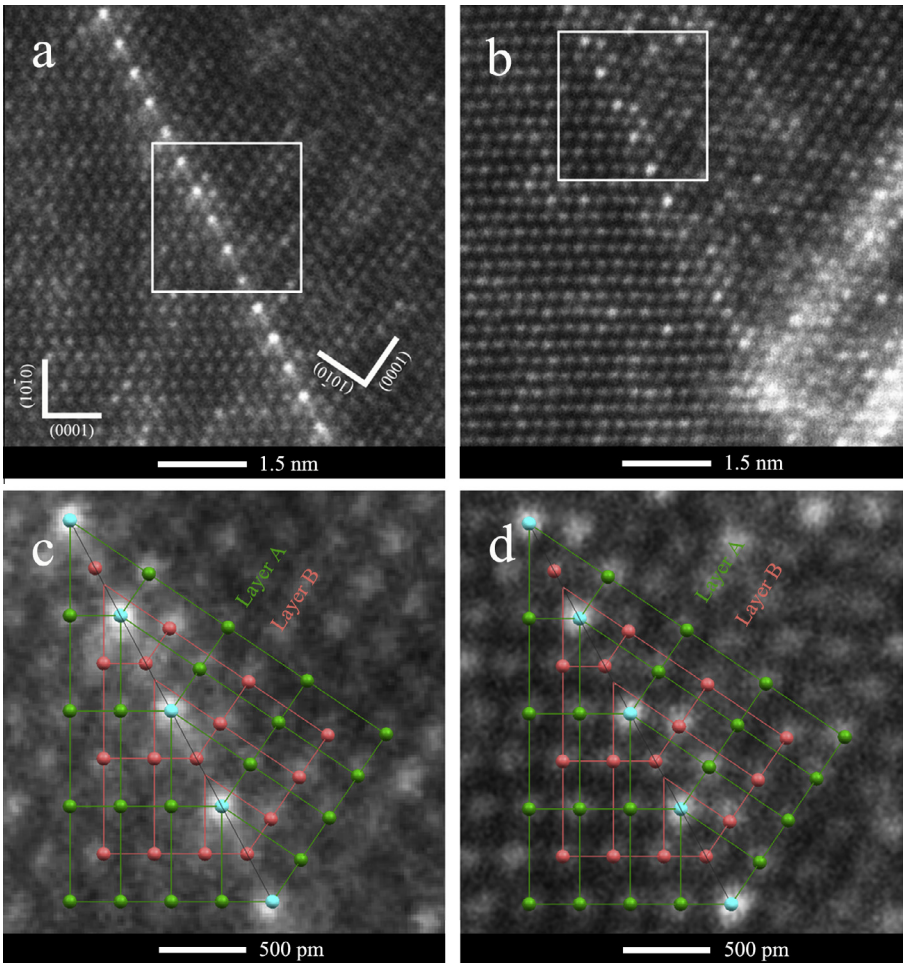


**Fig. 3.** HAADF-STEM images of TBI with the incident beam parallel to the $[11\bar{2}0]$ axis: (a) and (c) Mg–Gd–Y alloys and enlarged image marked by the atomic model; (b) and (d) Mg–Gd–Y–Ag alloy and enlarged image marked by the atomic model. Green and pink spheres representing atoms in layer A and B of Mg crystal, respectively, and turquoise spheres representing the segregated solute atoms. (For interpretation of the references to colour in this figure legend, the reader is referred to the web version of this article.)

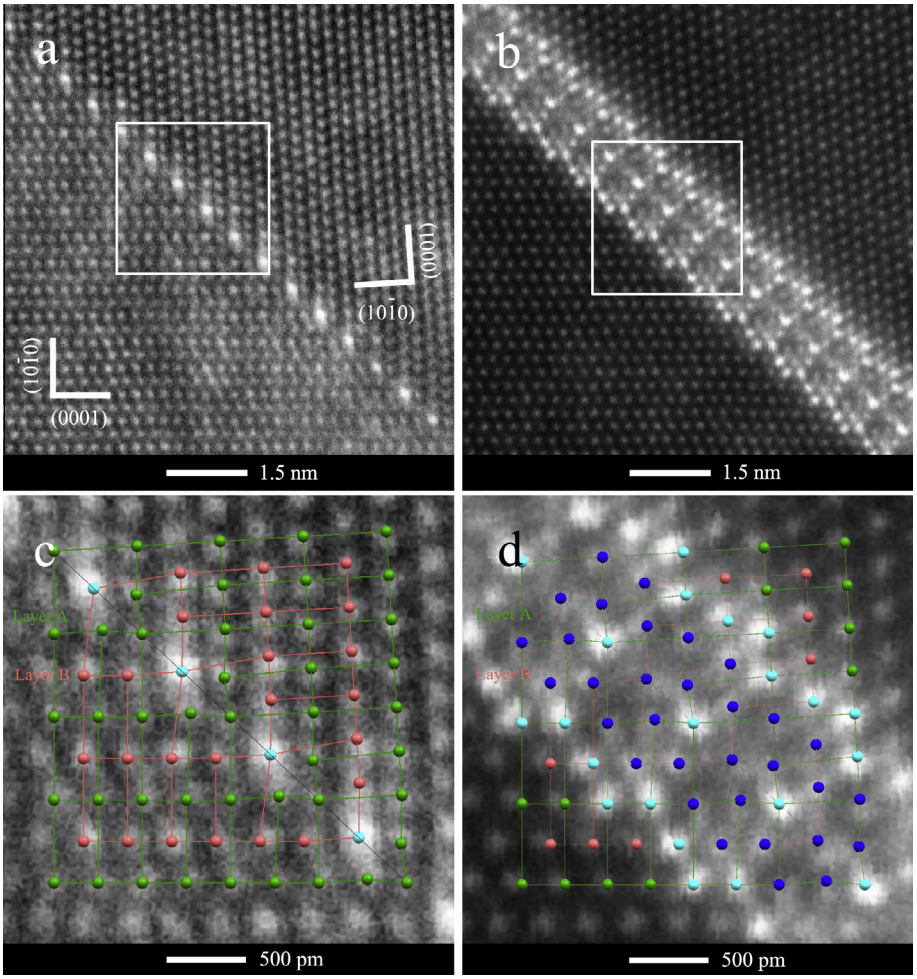


**Fig. 4.** HAADF-STEM images of TBII with the incident beam parallel to the [11$\bar{2}$0] axis: (a) and (c) Mg–Gd–Y alloys annealed for 30 min. at 250 °C and the enlarged image by the atomic model; (b) and (d) Mg–Gd–Y–Ag alloy and the enlarged image marked by the atomic model. Green and pink spheres represent atoms in layers A and B of the Mg lattice, respectively, turquoise spheres represent the brightest spots, and blue spheres represent the spots with weaker brightness. (For interpretation of the references to colour in this figure legend, the reader is referred to the web version of this article.)

common and important mechanism for plastic deformation in hexagonal close-packed (hcp) metals [36]. There are theoretically at least seven twinning modes in hcp metals, involving different twinning planes, including {10$\bar{1}$1}, {10$\bar{1}$2}, {10$\bar{1}$3}, {11$\bar{2}$1}, {11$\bar{2}$2}, {11$\bar{2}$3} and {11$\bar{2}$4} [37]. Among them, {10$\bar{1}$1}, {10$\bar{1}$2} and {10$\bar{1}$3} twins (hereafter referred to TBI, TBII and TBIII, respectively) are the most common types observed in Mg alloys, which can be clearly observed in the [11$\bar{2}$0] zone axis [18]. For simplicity, all zone axes and crystal planes are hereafter those of the α-Mg matrix. Three types of lamellar structures were identified by using selected area diffraction as shown in Fig. 2. Classification of the lamellar structures in hot-rolled Mg–Gd–Y–(Ag)–Zr alloy is summarized in Table 1. The first lamellar structure is TBI with twin plane ($K_1$) of {10$\bar{1}$1} as shown in Fig. 2a and b. The angle between the twin {0001} planes and the matrix {0001} planes is ~125° as viewed from the [11$\bar{2}$0] zone axis. TBI is a compression twin since it typically forms under compressive stress [38]. Wu et al. observed TBI twins in an hcp Mg–Ti alloy [39], which was favored under compression. Fig. 2c and d shows the typical morphology of TBII, which is the predominant lamellar structure in hot-rolled samples. The angle between the two {0001} planes is 86° as marked in Fig. 2d. TBII is the most common twinning system observed in hcp Mg [40].

We also observed another kind of lamellar structure that had a unique orientation relative to the traditional twins, as shown in Fig. 2e and f. We define it as a special lamellar grain boundary (LGB), where neighboring grains shared the same [11$\bar{2}$0] zone axis. Such LGBs are easy to study under high-resolution TEM because atomic structures on both sides can be clearly imaged, which provides an opportunity to observe relevant structures on both sides of grain boundary. The misorientation angles across LGBs were found to vary. Table 1 lists at least four different angles observed in our alloy systems. In the following, the LGB with a typical angle of ~144° is used for segregation investigations. The formation mechanism of these LGBs will be discussed in Section 4.1.

### 3.2. Segregation at coherent twin boundaries

Shown in Fig. 3 are the atomic-resolution HAADF-STEM images of TBI in Mg–Gd–Y and Mg–Gd–Y–Ag alloys observed from the [11$\bar{2}$0] zone axis. After annealing at 250 °C for 30 min, single-line segregation along TBI occurred in both the 75% rolled Mg–Gd–Y and Mg–Gd–Y–Ag alloys, as shown in Fig. 3a and b, respectively. Models on their atomic structures are shown in the magnified images in Fig. 3c and d to demonstrate the different Z-contrasts caused by different elements. The green and pink spheres represent atoms in layers A and B in magnesium matrix, respectively. Turquoise spheres represent solute atoms that have bright contrast in HAADF-STEM image. It shows that the atoms at the twin interface are not perfectly close-packed. The atoms in

layer A are close to the exact lattice sites, while atoms in layer B are located in compression sites [18]. Compression sites are caused by lattice distortion that makes their distance to surrounding atoms smaller. In contrast, extension sites are those that have larger space than sites in perfect lattice. Both alloys exhibit similar segregation behaviors at the interface of TBI: Mg atoms on layer A are replaced by solute atoms while no replacement occurred on layer B.

In contrast, TBII shows different segregation phenomena in the alloys with and without Ag. Fig. 4a and b shows the HAADF-STEM images of TBII in Mg–Gd–Y and Mg–Gd–Y–Ag alloys after annealing, respectively. Corresponding atomic models are provided in Fig. 4c and d, which use the same color schemes as those in Fig. 3. The blue atoms represent spots with weaker brightness. The morphology of interfacial segregation at TBII of Mg–Gd–Y alloy is still single-line shaped, as shown in Fig. 4a, while the alloy containing Ag shows a unique segregation with periodic structures as shown in Fig. 4b. From the [11$\bar{2}$0] direction, the structure looks like a "spine" along the twin boundary. It is clear from the figure that the central column and two side columns of atoms are brightest, while the atoms between them are dimmer but still brighter than Mg atoms in the matrix. It has been reported that segregated atoms increase the pinning effect on the twin boundary [18]. The number of segregated atom sites in Mg–Gd–Y–Ag alloy (Fig. 4b) is much larger than those in the alloy without Ag (Fig. 4a), suggesting that Ag helps to stabilize the twin boundary. The atomic model in Fig. 4c and d indicates that the atomic stacking of TBII is not perfect. The compression sites are located in layer A, which is different from TBI. By measuring the distance of neighboring atoms, the compression sites are found to occupy more space in TBII than those in TBI. Another crucial difference is that layer B in TBII is located in extension sites, which is not observed in TBI. The atomic models of Mg–Gd–Y and Mg–Gd–Y–Ag alloys indicate that the addition of Ag also changes the positions where atomic replacement occurs in TBII.

In order to confirm the effects of Ag on the interfacial segregation directly, EDS mapping was carried out at twin boundaries as shown in Fig. 5. For simple comparison, a region containing both TBI and TBII was selected for the mapping as shown in Fig. 5a. Fig. 5c and d shows significant segregation of Gd and Ag in both

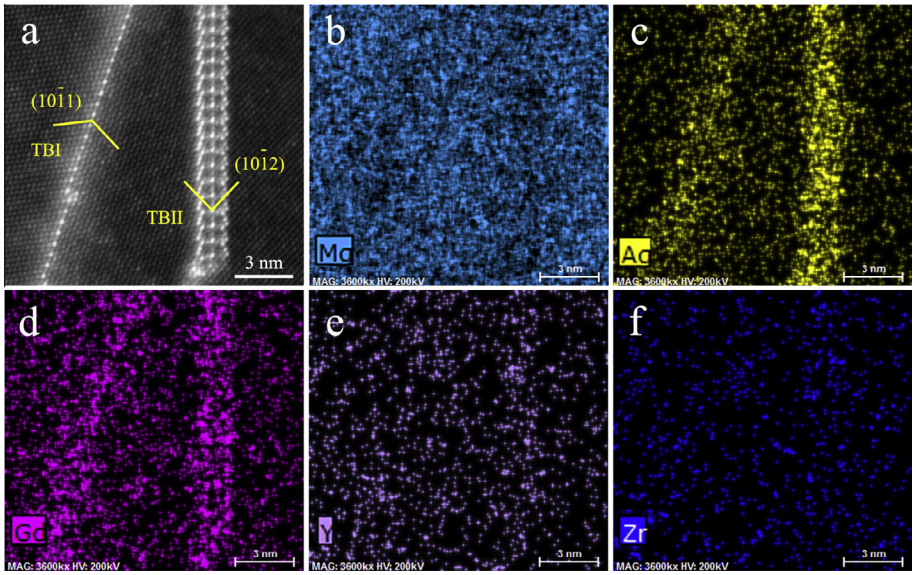


**Fig. 5.** EDS chemical mapping of the twin boundary segregations in Mg–Gd–Y–Ag–Zr alloy: (a) the corresponding HAADF-STEM image, (b) Mg-Kα; (c) Ag-Kα; (d) Gd-Kα; (e) Y-Kα; and (f) Zr-Kα.

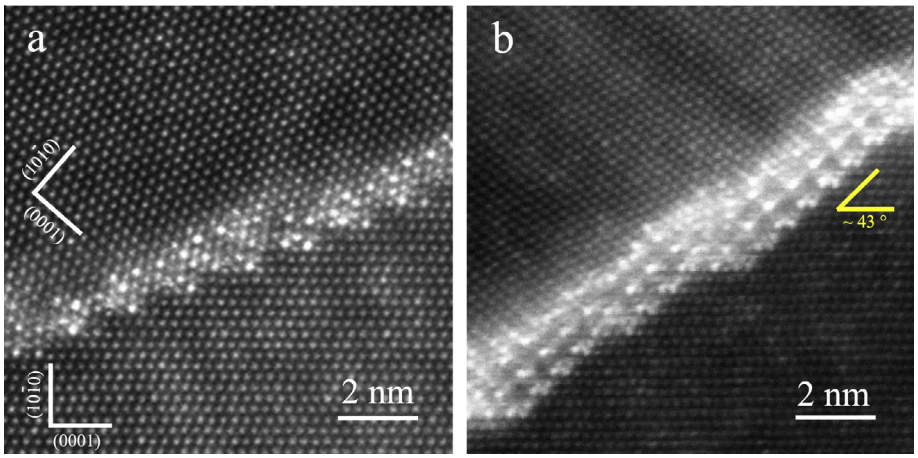


**Fig. 6.** HAADF-STEM images of grain boundaries with the incident beam parallel to the [11$\bar{2}$0] axis: (a) Mg–Gd–Y alloy; (b) Mg–Gd–Y–Ag alloy.

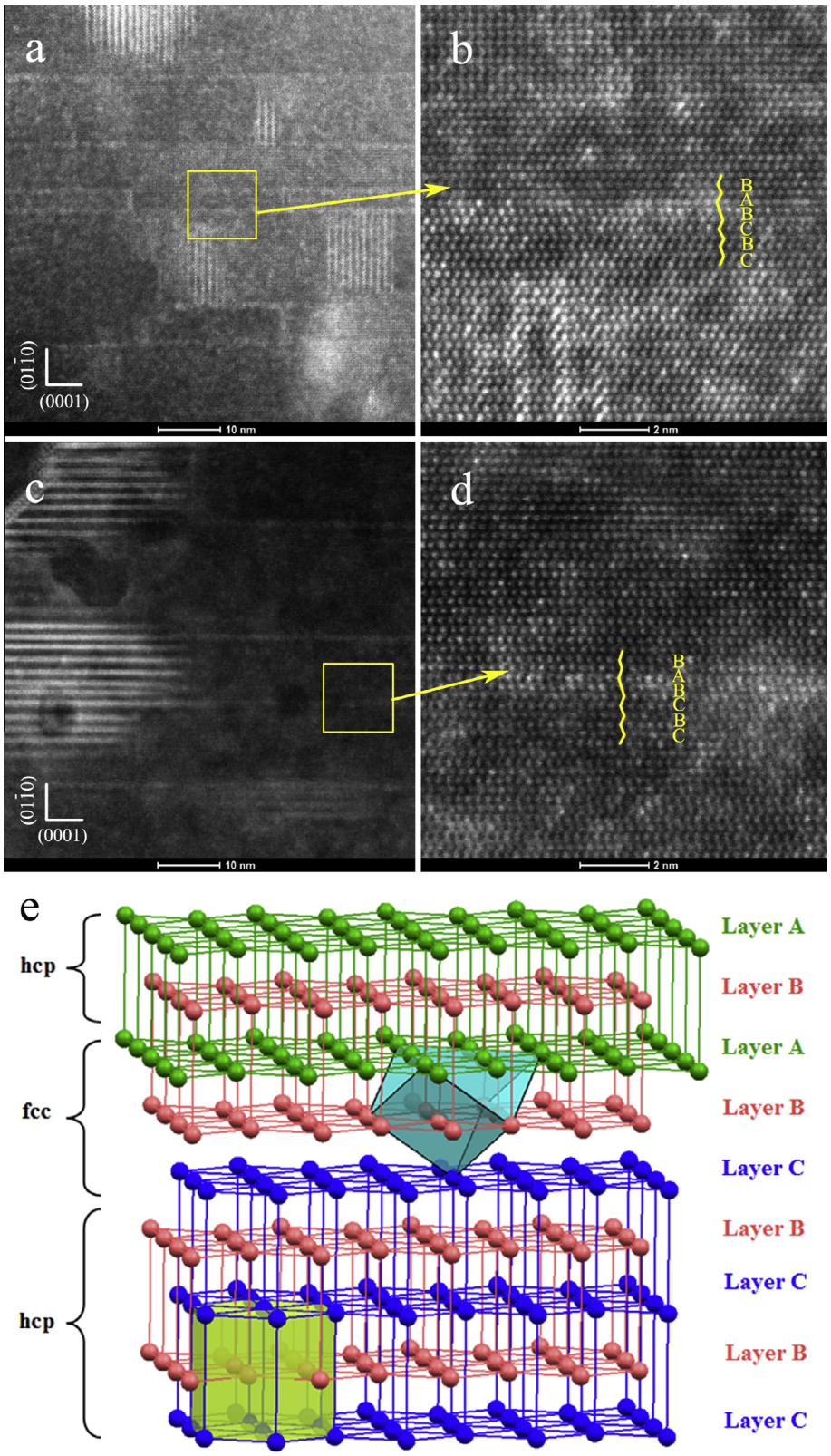


**Fig. 7.** HAADF-STEM images of segregation at stacking faults: (a) and (b) Mg–Gd–Y–Zr alloy, (c) and (d) Mg–Gd–Y–Ag–Zr alloy, and (e) atomic model of I1stacking faults.

TBI and TBII in Mg–Gd–Y–Ag alloy. In contrast, Y is not obviously segregated to either twin boundaries (Fig. 5e). Fig. 5f indicates that Zr was not segregated either, which is consistent with a literature report [41].

### 3.3. Segregation at grain boundaries

Fig. 6 shows the segregation at lamellar grain boundaries (LGBs) of Mg–Gd–Y and Mg–Gd–Y–Ag alloys. In order to make valid

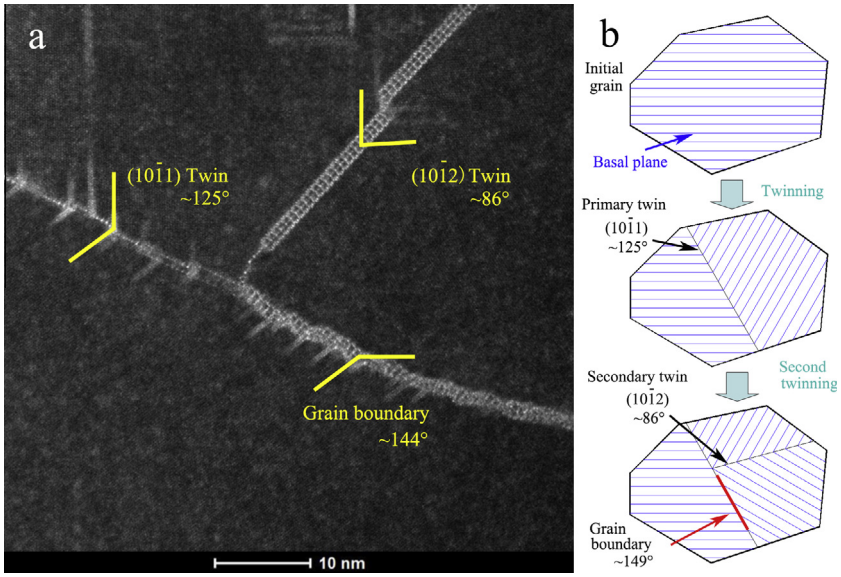


**Fig. 8.** (a) HAADF-STEM images of grain boundaries with the incident beam parallel to the [11$\bar{2}$0] axis, and (b) schematic of formation process of special grain boundary.

comparisons, the same grain boundary angle of ~144° is chosen for comparison in both alloys. Different segregation phenomena are observed at the grain boundaries in the alloys with and without Ag, which is similar to the observations for TBII. The alloy with Ag shows spinal-shaped segregation structures, however, this "spine" at the LGB is not continuous, and appears to be pieced together of several parallel segments. It appears to try to follow both the (10$\bar{1}$2) plane as on the TBII and the LGB, but the (10$\bar{1}$2) plane does not coincide with the LGB, which leads to the segmented feature shown in Fig. 6b. This observation also indicates the importance of the (10$\bar{1}$2) twin boundary (TBII) in the formation of the spinal-shaped segregation.

### 3.4. Segregation at stacking faults

Fig. 7a and c shows the low magnification HADDF-STEM images of 75% rolled Mg–Gd–Y and Mg–Gd–Y–Ag samples. A high density of stacking faults appeared in both alloys, which tend to be generated in twins or lamellar grains mentioned above. Jian et al. reported the role of the nano-spaced stacking faults to improve the mechanical properties of magnesium alloys [10,11]. The yield strength follows a linear relationship with the reciprocal of average spacing of stacking faults [10]. In this work, the spacing of stacking faults in the two alloys is in the range of 10–20 nm. High resolution images in Fig. 7b and d show that the stacking faults in the alloys are mainly I1 type, which has a stacking sequence of ABABABCBCBCB. I1 stacking faults introduce a thin three-layer of face-center cubic (fcc) stacking structure into the hcp matrix as shown in Fig. 7e. After annealing at 250 °C for 0.5 h, Suzuki segregation of solute atoms to the three fcc layers of stacking faults occurred, which is also reported in Mg–Y–Zn alloys [19]. The Suzuki segregation on stacking faults is different from the reported LPSO structure in Mg alloys [8]. First, the structure of Suzuki segregation only appeared in the local fcc layers at the stacking faults. Furthermore, the Suzuki segregation does not show any periodicity along the *c*-axis as in the LPSO periodic structures.

**Table 2**
Possible angle of LGBs induced by two and three twinning events.

| The number of twins | Twining type | Possible angle of LGB |
|---|---|---|
| 2 – twinning | TBI + TBI | 110° |
| | TBII + TBII | 172° |
| | TBI + TBII | 141° and 149° |
| 3 – twinning | TBI + TBI + TBI | 165° |
| | TBII + TBII + TBII | 102° |
| | TBI + TBII + TBII | 117° and 147° |
| | TBI + TBI + TBII | 164° and 156° |

## 4. Discussion

### 4.1. Proposed formation mechanism for special lamellar grain boundary

Grain boundaries with neighboring grains sharing the same [11$\bar{2}$0] zone axis are widely observed in our deformed samples. We hypothesize that they were formed by multiple twinning. Note that the size of a virgin grain may be too large (see Fig. 1) to be fully captured by TEM, but local feature analysis could shed some light on this issue. Fig. 8a shows a local triple-junction area including TBI, TBII and the resulting LGB. The formation of such morphology from the virgin grain is schematically illustrated in Fig. 8b. First, assuming that there is an initial grain that has a [11$\bar{2}$0] zone axis perpendicular to the page, then the horizontal

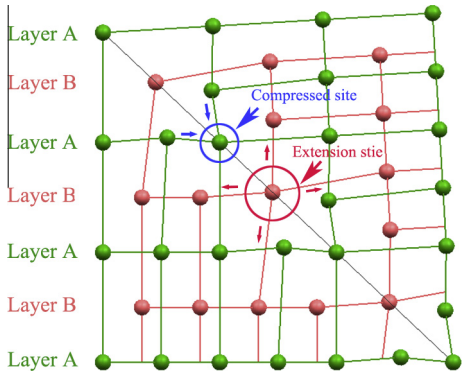


**Fig. 9.** Crystal structure of TBII in the direction of (11$\bar{2}$0) α plane.

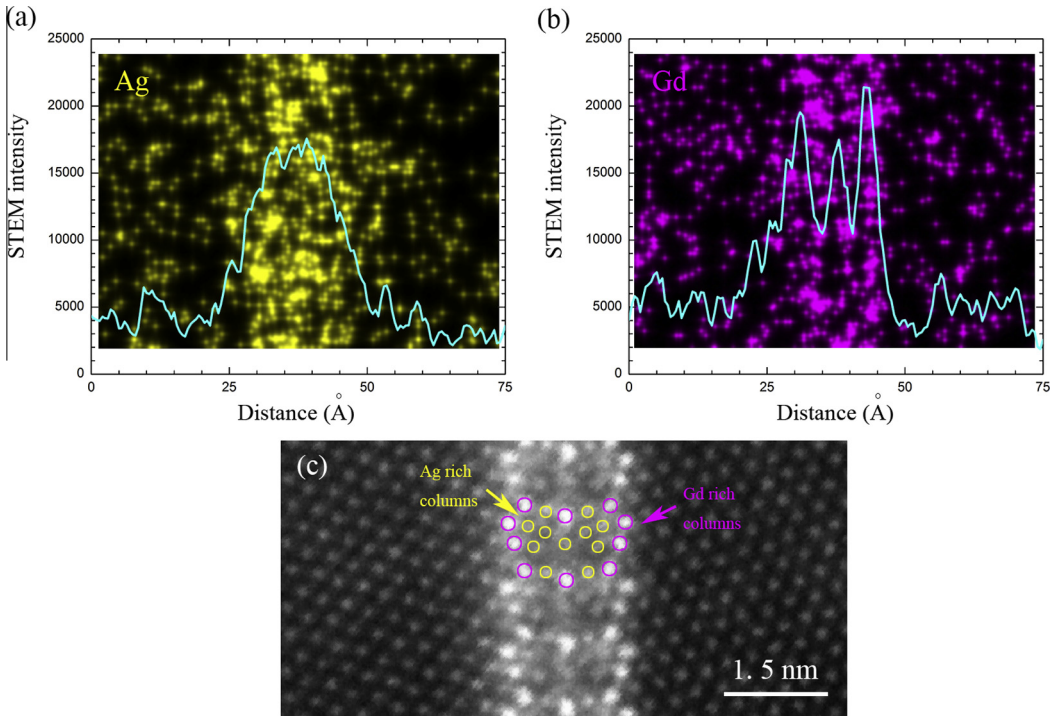


**Fig. 10.** Integration of the STEM intensity of (a) Ag and (b) Gd across a TBII, and (c) HAADF-STEM image of TBII of Mg–Gd–Y–Ag alloy with the incident beam parallel to the [1 1 $\bar{2}$ 0] zone axis. The yellow circles represent Al-enriched sites and the purple circles represent the Gd-enriched sites. (For interpretation of the references to colour in this figure legend, the reader is referred to the web version of this article.)

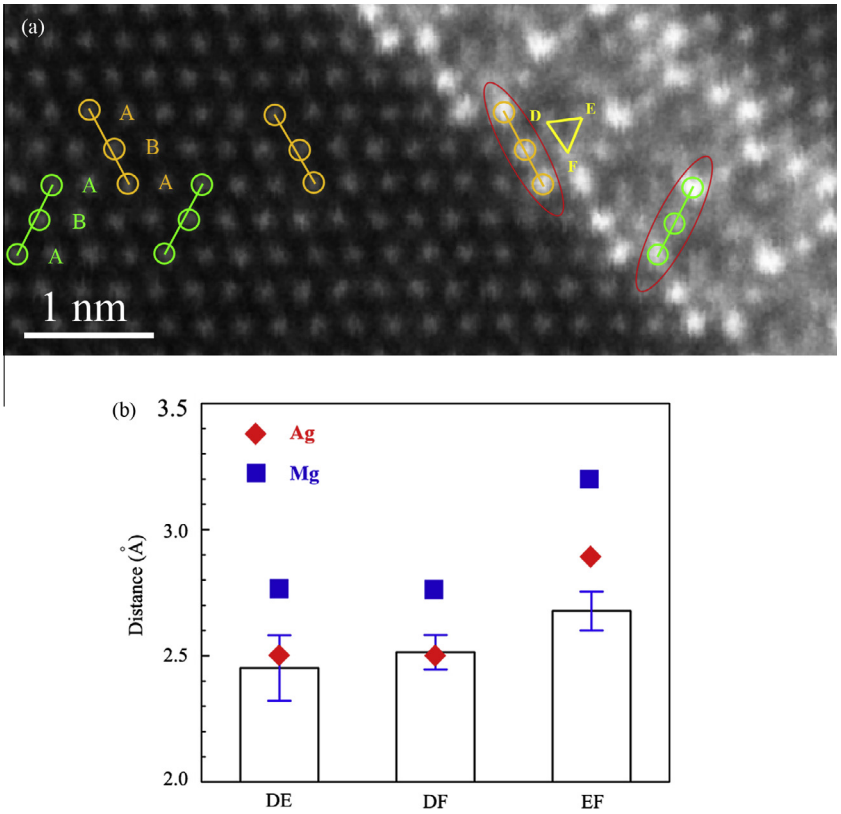


**Fig. 11.** (a) HAADF-STEM image of TBII of Mg–Gd–Y–Ag alloy with the incident beam parallel to the [1 1 $\bar{2}$ 0] zone axis, and (b) statistical distance of DE, DF and EF.

**Table 3**
Twin boundaries energy in Mg [41].

| Twin boundary | $\Gamma(10\bar{1}1)$ | $\Gamma(10\bar{1}2)$ | $\Gamma(10\bar{1}3)$ | $\Gamma(11\bar{2}1)$ | $\Gamma(11\bar{2}2)$ | $\Gamma(11\bar{2}3)$ | $\Gamma(11\bar{2}3)$ |
|---|---|---|---|---|---|---|---|
| Energy (mJ/m$^2$) | 143 | 189 | ~189 | 148 | 145 | ~145 | ~145 |

blue lines in Fig. 8b represent the basal planes of the grain. When the alloy is subjected to rolling, a primary twin forms, which changes the orientation of the right part of TBI as shown in Fig. 8b. Further deformation leads to the formation of the secondary twin in the primary twin. Thus, the right part of the grain will be re-oriented again due to the secondary twinning. Now the red marked boundary becomes one of the special LGBs observed in this study, which has $[11\bar{2}0]$ zone axis for both sides with a misorientation angle of 149°. If the basal planes interact with other defects such as dislocations, the resulting misorientation angles could be slightly different from the predicted value, as observed in this study. As mentioned earlier, the misorientation angles may vary, depending on the type and number of multiple twinning modes. Table 2 lists all possible angles produced by two and three twinning events. Note that there may be other cases where grain boundary angle is formed by more than three consecutive twinning events.

### 4.2. Proposed mechanism of segregation at interfaces

As shown in Fig. 9, there are two types of lattice sites alternating along the TBII: the compression site and extension site. The space of compression site is smaller than a normal Mg atom would occupy, whereas the extension site is larger. Therefore, TBII is an interface with alternative tensile and compressive elastic strains. It has been reported that the size of solute atoms affects the segregations at twin boundaries [18]: solute atoms larger than Mg tend to segregate to the tension sites, while those smaller than Mg tend to segregate to the compression sites. In our case, if the same segregation trend is followed, the large Gd and Y (0.188 nm) atoms should segregate to tension sites, while the smaller Ag atoms should segregate to the compression sites.

A careful EDS analysis is carried out to investigate the segregation of the alloy elements. Fig. 10a and b shows the integration of the brightness contrast along a TBII. As shown in Fig. 10a, Ag atom distribution has only one peak within the width of ~1.5 nm, which is very close to the width of spinal-shaped segregation in TBII. In other words, Ag is almost uniformly distributed across TBII. However, the distribution of Gd has three apparent peaks across TBII (Fig. 10b), indicating three separate Gd atom concentration columns across the TBII. It should be noted that the intensity of the middle peak is slightly weaker than the two side peaks. Based on this information, the atomic structure of alloy segregation can be schematically illustrated in Fig 10c. Combining with the fact that Gd has the highest atomic number of the three elements in the alloy (64 for Gd, 47 for Ag, and 12 for Mg), it is reasonable to assume that the brightest spots correspond to atomic sites of higher Gd concentrations, as indicated by purple circles in Fig. 10c. The atomic sites between them have median brightness and are probably Ag-enriched, as marked by yellow circles in Fig 10c.

The Ag enrichment appears to affect the lattice structure of local area near TBII. As is shown in Fig. 11a, the area far away from twin boundary follows an ABAB … hcp stacking sequence. However, three adjacent layers of atoms in the area near twin boundary appear to arrange in a straight line as marked by the red ellipse. This kind of atomic stacking is similar to that in fcc lattice with a packing sequence of ABCABC … ABC. Statistics on the interatomic distances between three typical Ag-rich columns of D, E and F is shown in Fig. 11b, which was analyzed from 36 different atom pairs along TBII. Their values are compared with that of pure Ag and Mg, as shown in Fig. 10b and c. It is obvious that they match better with pure Ag than pure Mg. This further indicates that the atomic packing in the spinal-shaped segregation is close to that of fcc Ag, possibly due to the high Ag content in this area.

The above observations indicate that segregation varies with interface types. Capolungo [42] reported first-principle calculations of the twin boundary energies for seven different types of twins in Mg (shown in Table 3). The stacking fault energy on the basal plane in Mg is $\Gamma^{SF} = 14$ mJ/m$^2$ (which is the upper value of theoretical prediction) [43,44]. It is generally accepted that grain boundary energy is usually higher than coherent twin boundary energy [45]. Therefore, the sequence of interfacial energies concerned in this paper is: $\Gamma^{LGB} > \Gamma^{TBII} > \Gamma^{TB}I > \Gamma^{SF}$. The periodic spinal-shaped segregation only occurs in TBII and LGBs with higher energies, which suggests that with Ag addition, spinal-shaped segregation only occurs in interfaces with high energies.

## 5. Conclusion

This study revealed interfacial segregation of solute atoms to interfaces including grain boundaries, twin boundaries, and stacking faults in Mg–Gd–Y–(Ag)–Zr alloys using atomic-resolution HAADF-STEM imaging and EDS mapping. Ag addition was found to significantly affect segregations at high-energy interfaces. The following are new understandings gained from this study:

1. Ag-assisted segregation at $\{10\bar{1}2\}$ twin boundaries (TBII) and lamellar grain boundaries (LGB) exhibits a new periodic spinal-shaped structure that is different from the single-lined segregation in the alloy without Ag. The segregation at $\{10\bar{1}1\}$ twin boundaries (TBI) shows the same periodic single-line segregation with or without Ag addition. The segregation at I1 stacking faults is random without any periodicity in both Mg–Gd–Y and Mg–Gd–Y–Ag alloys.
2. EDS mapping revealed significant segregation of Gd and Ag at both TBI and TBII in Mg–Gd–Y–Ag alloy. Ag atoms are uniformly distributed across TBII, while the Gd atoms have three distribution peaks. In the spinal-shaped segregation at TBII, the brightest spots are proposed as Gd-rich columns, and the median-brightness spots between them are Ag-rich columns. The addition of Ag induced many local quasi-fcc structures.
3. Interfacial energy affects the interfacial segregation. The sequence of interfacial energy in this paper is: $\Gamma^{LGB} > \Gamma^{TBII} > \Gamma^{TB}I > \Gamma^{SF}$. The periodic spinal-shaped segregation only occurs in TBII and LGBs with higher energies, and is absent at lower energy TBI and I1 stacking faults.
4. The lamellar grain boundaries with unique orientation were found in rolled Mg alloys, which was proposed formed by multiple twinning. Possible mis-orientation angles of LGB are 110°, 141°, 149° and 172° after secondary twinning, and are 102°, 117°, 147°, 156°, 164°and 165° after tertiary twinning.

## Acknowledgements

This work was supported by the National Natural Science Foundation of China (NSFC) under Grant Nos. 51404151, 51374145, 51074106, 50674067, Program from the Ministry of

Education of PR China, National Key Technology R & D Program of China under Grant No. 2011BAE22B01-5, China Postdoctoral Science Foundation funded project (2014M561466), Sponsored by Shanghai Postdoctoral Scientific Program (14R21411000), the Science and Technology Commission of Shanghai Municipality under Grant Nos. 09JC1408200 and 06SR07104, as well as the U.S. Army Research Office under Grant No. W911NF-12-1-0009. The authors thank W. Guo and W.W. Jian for support during material preparation. B. Ye, C.X. Huang and J. Moering for good suggestion of paper revision and theory discussion.

## References

[1] T.M. Pollock, Science 328 (2010) 986.
[2] S.R. Agnew, J.F. Nie, Scripta Mater. 63 (2010) 671.
[3] W. Guo, Q.D. Wang, B. Ye, M.P. Liu, T. Peng, X.T. Liu, H. Zhou, Mater. Sci. Eng., A 540 (2012) 115.
[4] H. Zhou, Q.D. Wang, B. Ye, W. Guo, Mater. Sci. Eng., A 576 (2013) 101.
[5] H. Wang, Q.D. Wang, D.D. Yin, J. Yuan, B. Ye, Mater. Sci. Eng., A 578 (2013) 150.
[6] L. Mao, L. Shen, J.L. Niu, J. Zhang, W.J. Ding, Y. Wu, R. Fan, G.Y. Yuan, Nanoscale 5 (2013) 9517.
[7] W.J. Kim, H.G. Jeong, H.T. Jeong, Scripta Mater. 61 (2009) 1040.
[8] J.F. Nie, K. Oh-ishi, X. Gao, K. Hono, Acta Mater. 56 (2008) 6061.
[9] E. Abe, Y. Kawamura, K. Hayashi, A. Inoue, Acta Mater. 50 (2002) 3845.
[10] W.W. Jian, G.M. Cheng, W.Z. Xu, H. Yuan, M.H. Tsai, Q.D. Wang, C.C. Koch, Y.T. Zhu, S.N. Mathaudhu, Mater. Res. Lett. 1 (2013) 61.
[11] W.W. Jian, G.M. Cheng, W.Z. Xu, C.C. Koch, Q.D. Wang, Y.T. Zhu, S.N. Mathaudhu, Appl. Phys. Lett. 103 (2013).
[12] P. Gu, Y.T. Zhu, S.N. Mathaudhu, Philos. Mag. Lett. 95 (2015) 58.
[13] T. Homma, N. Kunito, S. Kamado, Scripta Mater. 61 (2009) 644.
[14] H. Zhou, W.Z. Xu, W.W. Jian, G.M. Cheng, X.L. Ma, W. Guo, S.N. Mathaudhu, Q.D. Wang, Y.T. Zhu, Philos. Mag. 94 (2014) 2403.
[15] S.M. He, X.Q. Zeng, L.M. Peng, X. Gao, J.F. Nie, W.J. Ding, J. Alloys Compd. 427 (2007) 316.
[16] M. Bugnet, A. Kula, M. Niewczas, G.A. Botton, Acta Mater. 79 (2014) 66.
[17] J.P. Hadorn, T.T. Sasaki, T. Nakata, T. Ohkubo, S. Kamado, K. Hono, Scripta Mater. 93 (2014) 28.
[18] J.F. Nie, Y.M. Zhu, J.Z. Liu, X.Y. Fang, Science 340 (2013) 957.
[19] Z.Q. Yang, M.F. Chisholm, G. Duscher, X.L. Ma, S.J. Pennycook, Acta Mater. 61 (2013) 350.
[20] J.P. Buban, K. Matsunaga, J. Chen, N. Shibata, W.Y. Ching, T. Yamamoto, Y. Ikuhara, Science 311 (2006) 212.
[21] P.V. Liddicoat, X.Z. Liao, Y.H. Zhao, Y.T. Zhu, M.Y. Murashkin, E.J. Lavernia, R.Z. Valiev, S.P. Ringer, Nat. Commun. 1 (2010) 63.
[22] M. Yamasaki, T. Anan, S. Yoshimoto, Y. Kawamura, Scripta Mater. 53 (2005) 799.
[23] M. Yamasaki, M. Sasaki, M. Nishijima, K. Hiraga, Y. Kawamura, Acta Mater 55 (2007) 6798.
[24] T. Honma, T. Ohkubo, S. Kamado, K. Hono, Acta Mater. 55 (2007) 4137.
[25] Y. Kawamura, T. Kasahara, S. Izumi, M. Yamasaki, Scripta Mater. 55 (2006) 453.
[26] X. Hui, W. Dong, G.L. Chen, K.F. Yao, Acta Mater. 55 (2007) 907.
[27] Y.M. Zhu, A.J. Morton, J.F. Nie, Acta Mater. 58 (2010) 2936.
[28] K. Yamada, H. Hoshikawa, S. Maki, T. Ozaki, Y. Kuroki, S. Kamado, Y. Kojima, Scripta Mater. 61 (2009) 636.
[29] Q.D. Wang, J. Chen, Z. Zhao, S.M. He, Mater. Sci. Eng., A 528 (2010) 323.
[30] Z.C. Wang, M. Saito, K.P. McKenna, L. Gu, S. Tsukimoto, A.L. Shluger, Y. Ikuhara, Nature 479 (2011) 380.
[31] A. Hirata, T. Fujita, Y.R. Wen, J.H. Schneibel, C.T. Liu, M.W. Chen, Nat. Mater. 10 (2011) 922.
[32] H. Zhou, Q.D. Wang, J. Chen, B. Ye, W. Guo, Trans. Nonferr. Metals Soc. China 22 (2012) 1891.
[33] W.Z. Xu, Y.F. Zhang, G.M. Cheng, W.W. Jian, P.C. Millett, C.C. Koch, S.N. Mathaudhu, Y.T. Zhu, Nat. Commun. 4 (2013).
[34] K.H. Kim, B.C. Suh, J.H. Bae, M.S. Shim, S. Kim, N.J. Kim, Scripta Mater. 63 (2010) 716.
[35] M.T. Perez-Prado, J.A. del Valle, J.M. Contreras, O.A. Ruano, Scripta Mater. 50 (2004) 661.
[36] C.X. Huang, K. Wang, S.D. Wu, Z.F. Zhang, G.Y. Li, S. Li, Acta Mater. 54 (2006) 655.
[37] J. Wang, J.P. Hirth, C.N. Tome, Acta Mater. 57 (2009) 5521.
[38] J.W. Christian, S. Mahajan, Prog. Mater. Sci. 39 (1995) 1.
[39] X.L. Wu, K.M. Youssef, C.C. Koch, S.N. Mathaudhu, L.J. Kecskes, Y.T. Zhu, Scripta Mater. 64 (2011) 213.
[40] Q. Yu, L. Qi, K. Chen, R.K. Mishra, J. Li, A.M. Minor, Nano Lett. 12 (2012) 887.
[41] M. Shahzad, L. Wagner, Scripta Mater. 60 (2009) 536.
[42] L. Capolungo, I.J. Beyerlein, Phys. Rev. B 78 (2008) 024117.
[43] M.I. Baskes, R.A. Johnson, Modell. Simul. Mater. Sci. Eng. 2 (1994) 147.
[44] W.Y. Hu, B.W. Zhang, B.Y. Huang, F. Gao, D.J. Bacon, J. Phys. Condens. Mat. 13 (2001) 1193.
[45] L. Lu, Y.F. Shen, X.H. Chen, L.H. Qian, K. Lu, Science 304 (2004) 422.